Commun. Comput. Phys.
doi: 10.4208/cicp.OA-2018-0050

Vol. **25**, No. 1, pp. 189-217
January 2019

A Hybrid Numerical Simulation of Supersonic Isotropic Turbulence

Luoqin Liu[1], Jianchun Wang[2], Yipeng Shi[1], Shiyi Chen[1,2] and X. T. He[1,3,*]

[1] *State Key Laboratory for Turbulence and Complex Systems, Center for Applied Physics and Technology, College of Engineering, Peking University, Beijing 100871, China.*
[2] *Department of Mechanics and Aerospace Engineering, Southern University of Science and Technology, Shenzhen 518055, China.*
[3] *Institute of Applied Physics and Computational Mathematics, Beijing 100088, China.*

Received 20 February 2018; Accepted (in revised version) 25 April 2018

Abstract. This paper presents an extension work of the hybrid scheme proposed by Wang et al. [*J. Comput. Phys.* **229** (2010) 169-180] for numerical simulation of subsonic isotropic turbulence to supersonic turbulence regime. The scheme still utilizes an 8th-order compact scheme with built-in hyperviscosity for smooth regions and a 7th-order WENO scheme for highly compression regions, but now both in their conservation formulations and for the latter with the Roe type characteristic-wise reconstruction. To enhance the robustness of the WENO scheme without compromising its high-resolution and accuracy, the recursive-order-reduction procedure is adopted, where a new type of reconstruction-failure-detection criterion is constructed from the idea of positivity-preserving. In addition, a new form of cooling function is proposed, which is proved also to be positivity-preserving. With a combination of these techniques, the new scheme not only inherits the good properties of the original one but also extends largely the computable range of turbulent Mach number, which has been further confirmed by numerical results.

AMS subject classifications: 76F05, 76F50, 76F65

Key words: Supersonic turbulence, hybrid scheme, positivity-preserving ROR-WENO scheme, compact scheme.

1 Introduction

Compressible turbulence is of fundamental importance to a number of natural phenomena and industrial applications, including interstellar medium [1,2], solar winds [3], star-

*Corresponding author. *Email addresses:* lqliu@pku.edu.cn (L. Liu), wangjc@sustc.edu.cn (J. Wang), ypshi@coe.pku.edu.cn (Y. Shi), syc@pku.edu.cn (S. Chen), xthe@iapcm.ac.cn (X. T. He)

 ©2019 Global-Science Press

forming clouds in galaxies [4], high-temperature reactive flows [5], supersonic aircraft design [6] and inertial confinement fusion [7, 8]. With increasing computational resources, direct numerical simulations of incompressible turbulent flows have been routinely conducted for many canonical boundary conditions and geometries. Similar developments for compressible flows are desired in order to provide parameterizations needed for modeling complex compressible turbulence in relevant applications.

While the pseudo-spectral method for incompressible homogeneous isotropic turbulence in a periodic domain has been well established [9], such a standard method is no longer suitable for compressible turbulence at high Mach numbers due to the notorious Gibbs phenomenon [10]. This barrier can be overcome by either the shock-fitting approach [11] or the shock-capturing approach [12, 13]. Although the former guarantees more accurate representations of shocked flows, it is merely feasible in cases where the shock topology is extremely simple and no shock wave forms during the calculation. Since our present goal is to simulate compressible turbulence where shocklets form randomly, we discuss only the latter within the context of finite difference method (FDM), which can be mainly categorized into four classes, namely, the classical shock-capturing methods [13–20], the artificial viscosity methods [12, 21–24], the nonlinear filtering methods [25–28], and the hybrid methods [29–33]. For a review on these methods, the paper of [34] is highly recommended. At present paper, we only focus on the last one.

Briefly speaking, the hybrid methods are based on the idea of endowing a baseline spectral-like scheme with shock-capturing capability through local replacement with a classical shock-capturing scheme, where the shock sensor plays a key role. Along this direction, some progresses have been made in the past two decades. For example, Adams and Shariff [30] first considered a truly adaptive hybrid discretization, consisting of a baseline 5th-order compact upwind (CU) scheme coupled with a 5th-order essentially non-oscillatory (ENO) scheme, where the shock sensor is based on the local gradient of the flux vector components. Pirozzoli [31] expanded this method by transforming it into a fully conservative formulation, replacing the ENO scheme with weighted essentially non-oscillatory (WENO) scheme, and using the local density gradient as the shock sensor. This method was further improved by Ren et al. [32], who used the Roe type characteristic-wise reconstruction and introduced a complex weight function to gradually switch between CU scheme and WENO scheme at the interface. Zhou et al. [35] introduced a new family of CU scheme and combined this with WENO scheme. There are also several other studies that combine the usual, non-compact scheme and WENO scheme [36–38], but they have the very similar issues in shock detection and the interface treatments as discussed above.

Recently, Wang et al. [33] developed a novel hybrid scheme that is applicable to the numerical simulation of compressible isotropic turbulence with relatively high turbulent Mach number $M_t \lesssim 1.0$. This scheme utilizes a 7th-order WENO scheme for highly compression regions and an 8th-order compact central (CC) scheme for smooth regions, with the shock sensor being the shocklet detection algorithm given by Samtaney et al. [39]. In addition, a numerical hyperviscosity formulation is proposed to remove the alias er-

ror associated with the CC scheme without compromising its numerical accuracy. With this hybrid scheme (hereafter we call it Wang's scheme for short), the authors made a thorough study of subsonic isotropic turbulence, including but not limited to effect of shocklets on the velocity gradients [40], effects of local compressibility on the statistical properties and structures of velocity gradients [41], scaling and statistics of velocity structure functions [42], and shocklets-particle interaction [43], to name a few. For recent progress in this direction, please see the review of Chen et al. [44].

Needless to say, these progresses have deepened our understandings of compressible turbulence in the nonlinear subsonic regime with turbulent Mach number M_t less than 1 but not negligible. In sharp contrast, the nonlinear supersonic turbulence, where M_t is greater than unity, is still much less known. Although this configuration is unavoidable in astrophysics, hypersonic aerodynamics, and inertial confinement fusion, etc., it has been paid to of little attention because the lack of available tools. On the one hand, the nonlinear phenomena of the compressive mode are too strong such that traditional linear theories and asymptotic series expansions are no longer valid [45]. On the other hand, shocklets are more frequently generated from turbulent fluctuations as M_t increases [46], requiring higher challenges to the numerical methods. Although for Euler turbulence the highest M_t in numerical experiment has been as large as 17 [47], it is scarcely larger than unity for Navier-Stokes turbulence. For example, the largest M_t for this type of flow in literature is 0.6 for compact scheme [48], 0.8 for optimized WENO scheme [49], 0.885 for gas kinetic method [50], 1.02 for localized artificial method [51], and 1.03 for hybrid approach [42], etc. This embarrassed situation motivates us to develop a useful scheme to study the supersonic isotropic turbulence.

The paper is organized as follows. Section 2 presents the governing equations for compressible turbulent flow as well as some useful parameters. Section 3 describes the main techniques used to extend Wang's scheme to flows at larger values of turbulent Mach number. A series of numerical tests are then shown in Section 4 to illustrate the validation and extension of the new schemes. Finally, main conclusions are summarized in Section 5. To be self-contained, some well-known techniques involved in the present scheme are listed in the Appendix A.

2 Governing equations for compressible turbulence

Consider the compressible turbulence of calorically perfect gas driven and maintained by large-scale forcing term $\boldsymbol{f}$ and cooling function $-\Lambda$. The governing equations are

$$\partial_t \rho + \nabla\cdot(\rho\boldsymbol{u}) = 0, \tag{2.1}$$

$$\partial_t(\rho\boldsymbol{u}) + \nabla\cdot(\rho\boldsymbol{u}\boldsymbol{u}) = \rho\boldsymbol{f} - \nabla p + \nabla\cdot\boldsymbol{\tau}, \tag{2.2}$$

$$\partial_t(\rho E) + \nabla\cdot(\rho E\boldsymbol{u}) = -\rho\Lambda + \rho\boldsymbol{f}\cdot\boldsymbol{u} - \nabla\cdot(p\boldsymbol{u}) + \nabla\cdot(\boldsymbol{\tau}\cdot\boldsymbol{u}) - \nabla\cdot\boldsymbol{q}, \tag{2.3}$$

$$p = \rho RT, \tag{2.4}$$

where $\boldsymbol{u}$ is the fluid velocity, ρ,p,T are the density, pressure and temperature, E is total energy, R is the gas constant, $\boldsymbol{q}$ is the heat flux,

$$\boldsymbol{q}=-\kappa\nabla T \tag{2.5}$$

with κ and T being the heat conduction coefficient and temperature, and $\boldsymbol{\tau}$ is the viscous stress tensor (superscript T denotes matrix transpose),

$$\boldsymbol{\tau}\equiv 2\mu\mathbf{S}+\lambda\vartheta\mathbf{I},\quad \mathbf{S}\equiv\frac{1}{2}\left[\nabla\boldsymbol{u}+(\nabla\boldsymbol{u})^T\right]. \tag{2.6}$$

Here $\mathbf{I}$ is the unit tensor, $\vartheta=\nabla\cdot\boldsymbol{u}$ is the dilatation, μ and λ are the first (shear) and second dynamic viscosities, respectively. Under the Stokes assumption, $\lambda=-2\mu/3$. In addition, μ, as well as κ, can be modeled by Sutherland's law [52],

$$\frac{\mu}{\mu_0}=\frac{\kappa}{\kappa_0}=\frac{1.4042T_0}{T+0.4042T_0}\left(\frac{T}{T_0}\right)^{1.5}, \tag{2.7}$$

where subscript 0 denotes reference state. For air, $\mu_0=1.716\times10^{-5}\mathrm{kg/m\cdot s}$, $T_0=273.15\mathrm{K}$, and κ_0 can be obtained from the definition of Prandtl number, $Pr=\mu_0 c_p/\kappa_0=0.7$, where $c_p=$const. is the specific heat at constant pressure.

The governing equations for the kinetic energy $k=\boldsymbol{u}\cdot\boldsymbol{u}/2$ and internal energy $e=c_vT$ can be deduced from (2.2) and (2.3), and the results are

$$\partial_t(\rho k)+\nabla\cdot(\rho k\boldsymbol{u})=\rho\boldsymbol{f}\cdot\boldsymbol{u}+p\vartheta-\nabla\cdot(p\boldsymbol{u})+\nabla\cdot(\boldsymbol{\tau}\cdot\boldsymbol{u})-\varepsilon, \tag{2.8}$$

$$\partial_t(\rho e)+\nabla\cdot(\rho e\boldsymbol{u})=-\rho\Lambda-p\vartheta-\nabla\cdot\boldsymbol{q}+\varepsilon, \tag{2.9}$$

where ε is the viscous dissipation,

$$\varepsilon\equiv\boldsymbol{\tau}:\mathbf{S}=\mu_\theta\vartheta^2+\mu\omega^2-2\mu\nabla\cdot(\mathbf{B}\cdot\boldsymbol{u}). \tag{2.10}$$

Here, $\mu_\theta=\lambda+2\mu$ is the dilatational viscosity, $\omega=|\boldsymbol{\omega}|$ and $\boldsymbol{\omega}=\nabla\times\boldsymbol{u}$ are the vorticity magnitude and vector, respectively, and $\mathbf{B}$ is the surface-deformation tensor,

$$\mathbf{B}\equiv\vartheta\mathbf{I}-(\nabla\boldsymbol{u})^T,\quad \nabla\cdot\mathbf{B}=\mathbf{0}. \tag{2.11}$$

For isotropic turbulence, the average of (2.8) and (2.9) reduce to

$$\partial_t\langle\rho k\rangle=\langle\rho\boldsymbol{f}\cdot\boldsymbol{u}\rangle+\langle p\vartheta\rangle-\langle\varepsilon\rangle, \tag{2.12}$$

$$\partial_t\langle\rho e\rangle=-\langle\rho\Lambda\rangle-\langle p\vartheta\rangle+\langle\varepsilon\rangle. \tag{2.13}$$

Therefore, the forcing term $\boldsymbol{f}$ and the cooling function $-\Lambda$ have only direct effects on the kinetic energy and the internal energy, respectively. In sharp contrast, the pressure term can transform the internal energy to kinetic energy in expansion regions and transform

the kinetic energy to internal energy in compression regions. Nevertheless, for stationary isotropic flow, there is

$$\langle \rho \boldsymbol{f} \cdot \boldsymbol{u} \rangle = \langle \rho \Lambda \rangle, \tag{2.14}$$

namely, the kinetic energy added to the velocity field is balanced by the cooling rate.

Finally, we define some important parameters characterizing the compressible turbulence. The root-mean-square (rms) velocity $u_{\rm rms}$ and its spectrum $E(k)$ are defined as

$$\frac{3}{2}u_{\rm rms}^2 = \frac{1}{2}\langle \boldsymbol{u}(\boldsymbol{x},t)\cdot\boldsymbol{u}(\boldsymbol{x},t)\rangle = \int_0^\infty E(k)\mathrm{d}k, \tag{2.15}$$

where $\langle\cdot\rangle$ denotes ensemble average and k is the wavenumber. The longitudinal integral length scale L_I and the transverse Taylor-scale λ are defined by

$$L_I = \frac{\pi}{2u_{\rm rms}^2}\int_0^\infty \frac{E(k)}{k}\mathrm{d}k, \quad \lambda = \frac{\sqrt{3}u_{\rm rms}}{\left\langle (\partial_1 u_1)^2 + (\partial_2 u_2)^2 + (\partial_3 u_3)^2 \right\rangle^{1/2}}, \tag{2.16}$$

thus the typical eddy turnover time $T_e = L_I/u_{\rm rms}$. Then, the turbulent Mach number M_t and Taylor-microscale Reynolds number R_λ, the two most important dimensionless parameters in compressible isotropic turbulence, can be computed as

$$M_t = \sqrt{3}\frac{u_{\rm rms}}{\langle a\rangle}, \quad R_\lambda = \frac{\langle\rho\rangle u_{\rm rms}\lambda}{\langle\mu\rangle}, \tag{2.17}$$

where $a = \sqrt{\gamma RT}$ is the speed of sound and γ is the ratio of specific heat. Finally, the average viscous dissipation rate $\langle\varepsilon\rangle$ and Kolmogorov length scale η are computed as

$$\langle\varepsilon\rangle = \langle \boldsymbol{\tau}:\mathbf{S}\rangle, \quad \eta = \left(\frac{\langle\mu\rangle^3}{\langle\rho\rangle^2\langle\varepsilon\rangle}\right)^{1/4}. \tag{2.18}$$

These parameters are critical in the turbulence theory [53]. In addition, to represent the intermittency of turbulence, the skewness of velocity derivative S_3 is defined as

$$S_3 = \frac{\sqrt{3}\left\langle (\partial_1 u_1)^3 + (\partial_2 u_2)^3 + (\partial_3 u_3)^3 \right\rangle}{\left\langle (\partial_1 u_1)^2 + (\partial_2 u_2)^2 + (\partial_3 u_3)^2 \right\rangle^{3/2}}. \tag{2.19}$$

3 Review and implementation of the hybrid scheme

3.1 The hybrid scheme of Wang et al. (2010)

As remarked before, Wang et al. [33] combined the 7th-order WENO scheme (see [54] or Appendix A.1) for the shock regions and the 8th-order CC scheme (see [55] or Appendix A.2) for smooth regions to treat the advection terms in the governing equations

(2.1)-(2.3), where the shock front is identified by spatial points with highly negative local dilatation as defined by $\vartheta/\vartheta_{\rm rms}<-3$ [39]. Here $\vartheta_{\rm rms}$ denotes the rms value of dilatation. To depress potential oscillations due to the interface, additional six grid points are added on both sides in each spatial direction immediately outside the front. Thus, denoting $\boldsymbol{F}$ as the flux vector along x-direction (ref. (A.18) in Appendix A.3), they obtained

$$\frac{3}{8}\boldsymbol{F}'_{j-1}+\boldsymbol{F}'_j+\frac{3}{8}\boldsymbol{F}'_{j+1}=\frac{\boldsymbol{F}^{\rm Hybrid}_{j+1/2}-\boldsymbol{F}^{\rm Hybrid}_{j-1/2}}{\Delta x}, \tag{3.1}$$

where Δx is the uniform grid distance, $\boldsymbol{F}'$ is the x-derivative of the physical flux,

$$\boldsymbol{F}^{\rm Hybrid}_{j+1/2}\equiv\begin{cases}\boldsymbol{F}^{\rm Compact}_{j+1/2} & \text{for smooth regions,}\\ \boldsymbol{F}^{\rm WENO}_{j+1/2} & \text{for shock regions,}\\ \dfrac{1}{2}\left(\boldsymbol{F}^{\rm Compact}_{j+1/2}+\boldsymbol{F}^{\rm WENO}_{j+1/2}\right) & \text{at the joint,}\end{cases} \tag{3.2}$$

and

$$\begin{cases}\boldsymbol{F}^{\rm Compact}_{j+1/2}=\dfrac{398}{480}(\boldsymbol{F}_j+\boldsymbol{F}_{j+1})+\dfrac{23}{480}(\boldsymbol{F}_{j-1}+\boldsymbol{F}_{j+2})-\dfrac{1}{480}(\boldsymbol{F}_{j-2}+\boldsymbol{F}_{j+3}),\\ \boldsymbol{F}^{\rm WENO}_{j+1/2}=\dfrac{3}{8}\hat{\boldsymbol{F}}^{\rm WENO}_{j-\frac{1}{2}}+\hat{\boldsymbol{F}}^{\rm WENO}_{j+\frac{1}{2}}+\dfrac{3}{8}\hat{\boldsymbol{F}}^{\rm WENO}_{j+\frac{3}{2}}.\end{cases} \tag{3.3}$$

Similar to forcing incompressible turbulence [56], the solenoidal forcing $\boldsymbol{f}$ is constructed in the Fourier space by fixing the kinetic energy $E(k)$ per unit mass within the two lowest wave number shells, $0.5<k\leq 1.5$ and $1.5<k\leq 2.5$, to prescribed values consistent with the $k^{-5/3}$ kinetic energy spectrum. At the same time, to maintain a stationary state of compressible turbulence, energy is removed from the system through the cooling function $-\Lambda$ such that the mean internal energy is kept constant. In particular, the form of cooling function adopted is

$$\Lambda=aT^b, \tag{3.4}$$

where a and b are two parameters. Three different values of b, namely, $b=0,2,4$, were considered by [33], and no significant differences were found. The viscous term in the momentum equation and the viscous dissipation term in the energy equation were handled by a 6th-order non-compact central scheme, while the thermal diffusion term in the energy equation was still treated by an 8th-order CC scheme. The time marching was performed by the 2nd-order Runge-Kutta method [57].

3.2 Remarks on Wang's scheme

We remark that there are two possibilities that may degrade the high-resolution of Wang's scheme. One is that their scheme is not in truly conservation formulation as they asserted.

This can be seen clearly from (3.1), where the derivative of physical flux rather than numerical flux is solved. In fact, the scheme in truly conservation formulation is

$$\frac{3}{8}\hat{\boldsymbol{F}}_{j-\frac{1}{2}}+\hat{\boldsymbol{F}}_{j+\frac{1}{2}}+\frac{3}{8}\hat{\boldsymbol{F}}_{j+\frac{3}{2}}=\boldsymbol{F}^{\text{Hybrid}}_{j+1/2}, \tag{3.5}$$

where $\hat{\boldsymbol{F}}$ is the numerical flux and $\boldsymbol{F}^{\text{Hybrid}}_{j+1/2}$ is still given by (3.2). This can be obtained by following the tactic of Pirozzoli [31], of which the concept can be dated back to Lax [58]. Our numerical results show that this improvement has a negligible effect on the statistical properties of the flow field. However, for the instantaneous distribution of flow field there are some significant differences when shocklets exist (figure not shown). For example, when $M_t = 0.7$ there may be a relative larger discontinuity of the result obtained by the original scheme, which may be spurious and could lead to oscillations. Thus, we prefer (3.5) rather than (3.1) as our final formulation.

The other one is that the WENO scheme they adopted is based on the conservation-wise reconstruction rather than the characteristic-wise reconstruction, which may also lead to spurious oscillations. This can be improved by following the procedure of Ren et al. [32], of which the technique can be traced back to Harten et al. [59], where an implicit assumption, i.e., there is at least one smooth stencil, was used to prove the ENO property of the ENO scheme. This assumption, however, can never be satisfied in such problems where shock waves intersect with each other. To depress potential oscillations due to the violation of this assumption, Harten et al. [19] first recommended to use this kind of reconstruction. Similar to the first case, this improvement has also a negligible effect on the statistical properties of the flow field for $M_t < 1$. For extreme conditions (say, $M_t \gg 1$) where all flow processes are activated and so are their interactions, the scheme incorporated with conservation-wise reconstruction may fail due to numerical instability. Thus, we choose the characteristic-wise reconstruction, of which the details are given in Appendix A.3.

Characteristic-wise reconstruction alone, however, can never totally depress numerical oscillations and avoid blow-up. This is more serious in high-order schemes. To extend Wang's scheme to supersonic turbulence regime, therefore, more robust high-order shock-capturing schemes are desiring. Along this direction, some improved ENO/WENO schemes have been proposed, such as the TENO scheme [60] and WENO-AO scheme [61]. Their ideas are in common, both based on the fact that the lower-order stencils are more likely to have at least one smooth stencil than that of a higher-order one, and hence a lower-order scheme is taken when there is no smooth stencil of the higher-order. In fact, this procedure can be carried out recursively until the 1st-order scheme if there are discontinuities everywhere, which can be designed monotonic and of which the solution has been mathematically proved to exist at least for one-dimensional flow. This is the so-called recursive-order-reduction (ROR) method [62, 63], where the key ingredient is the reconstruction-failure-detection (RFD) criterion. However, the available criteria [62, 63] based on the density or pressure are somewhat empirical and may be problematic for

complex applications. To overcome this barrier, therefore, a new criterion based on the idea of positivity-preserving is constructed in § 3.3.

During our numerical tests, we encountered code blow-up even for the Godunov scheme [13] in the supersonic regime with the cooling function proposed by Wang et al. [33]. By numerical experiments and theoretical analysis, we realized that there are two reasons for this failure. One is that the simulation is sensitive to the initial conditions, and the other is that the cooling function itself is not positivity-preserving. The first one can be resolved by using the stationary flow data at a relatively smaller turbulent Mach number as initial conditions, while the second one is overcome by proposing a positivity-preserving cooling function (for details see § 3.4 below).

3.3 A positivity-preserving ROR-WENO scheme

It is well known that, for high-order WENO schemes non-physical negative density or pressure (failure of positivity) can occur due to interpolation errors at or near very strong discontinuities, which may cause blow-up of the numerical solution. Such pathological situations have indeed been observed in the Woodward-Colella problem and supersonic isotropic turbulence (results not shown here). To resolve this difficulty, two possible ways are available in literature.

The first one is to recursively reduce the order of WENO scheme, which was first adopted by Titarev and Toro [62] and is now called the ROR-WENO scheme [63]. Besides the traditional procedures involved in WENO scheme, it includes two extra steps:

1) Checking the reconstruction-failure-detection (RFD) criterion;

2) Reducing the order, say from r to $r-1$, recursively, until the criterion is *not* satisfied.

Evidently, the key ingredient of ROR-WENO scheme is the RFD criterion. Although the criterion proposed by Titarev and Toro [62] and/or that improved by Gerolymos et al. [63] have been successfully applied in some benchmark problems, they are not appropriate in our case since negative pressure or density can still occur due to very strong shocks/shocklets and thus make the scheme crash. The reason is that all these criteria are empirical to some extent and do not preserve positivity of density and pressure. Therefore, more robust criteria with strong mathematical foundation are urgently needed for the success of ROR-WENO scheme in the simulation of supersonic turbulence.

The second one is to resort to the so-called positivity-preserving method [64–66]. It first detects critical numerical fluxes which may lead to negative density and pressure, and then for such critical fluxes imposes a simple flux limiter by combining the high-order numerical flux with the 1st-order Lax-Friedrichs flux to satisfy a sufficient condition for preserving positivity. Some canonical problems involving vacuum or near vacuum suggest that this method, when applied on the WENO scheme, can be used to prevent positivity failure. We note that, the non-physical negative pressure and density due to interpolation errors at strong shocks have been used to determined the limiter function [64, 65], which might be problematic for the simulation of supersonic turbulence where

the shocks/shocklets are very strong and flow is far away from vacuum or near vacuum. Actually, our numerical experiments show that this method indeed *cannot* prevent the simulation of supersonic isotropic turbulence from blow-up. Nevertheless, the idea of positivity-preserving provides a physical-reasonable approach to construct more robust high-order shock-capturing schemes.

Realizing these disadvantages, here we propose a positivity-preserving ROR-WENO scheme, which is a combination of the advantages of the above two approaches. To illustrate its main idea, let us first write the general explicit $(2r-1)$th-order conservative scheme of the advection term of (A.18) with Euler-forward time integration as

$$\begin{aligned}\boldsymbol{U}_{i,j,k}^{n+1}=&\frac{1}{6}\left(\boldsymbol{U}_{i,j,k}^{n}-6\frac{\Delta t}{\Delta x}\hat{\boldsymbol{F}}_{i+\frac{1}{2},j,k}^{\mathrm{WENO}}\right)+\frac{1}{6}\left(\boldsymbol{U}_{i,j,k}^{n}+6\frac{\Delta t}{\Delta x}\hat{\boldsymbol{F}}_{i-\frac{1}{2},j,k}^{\mathrm{WENO}}\right)\\&+\frac{1}{6}\left(\boldsymbol{U}_{i,j,k}^{n}-6\frac{\Delta t}{\Delta y}\hat{\boldsymbol{G}}_{i,j+\frac{1}{2},k}^{\mathrm{WENO}}\right)+\frac{1}{6}\left(\boldsymbol{U}_{i,j,k}^{n}+6\frac{\Delta t}{\Delta y}\hat{\boldsymbol{G}}_{i,j-\frac{1}{2},k}^{\mathrm{WENO}}\right)\\&+\frac{1}{6}\left(\boldsymbol{U}_{i,j,k}^{n}-6\frac{\Delta t}{\Delta z}\hat{\boldsymbol{H}}_{i,j,k+\frac{1}{2}}^{\mathrm{WENO}}\right)+\frac{1}{6}\left(\boldsymbol{U}_{i,j,k}^{n}+6\frac{\Delta t}{\Delta z}\hat{\boldsymbol{H}}_{i,j,k-\frac{1}{2}}^{\mathrm{WENO}}\right).\end{aligned}\tag{3.6}$$

Note that positivity-preserving means that the density and pressure of $\boldsymbol{U}_{i,j,k}^{n+1}$ in the scheme (3.6) are positive when that of $\boldsymbol{U}_{i,j,k}^{n}$ are positive. Thus, a *sufficient* condition for preserving-positivity is that all terms within parentheses have positive density and pressure.

To see more clearly how the positivity-preserving idea works, we may take the flux $\boldsymbol{F}$ along x-direction as an example. First, define

$$\begin{cases}\boldsymbol{U}_{i,j,k}^{+}=\boldsymbol{U}_{i,j,k}^{n}-6\dfrac{\Delta t}{\Delta x}\hat{\boldsymbol{F}}_{i+\frac{1}{2},j,k}^{\mathrm{WENO}},\\ \boldsymbol{U}_{i+1,j,k}^{-}=\boldsymbol{U}_{i+1,j,k}^{n}+6\dfrac{\Delta t}{\Delta x}\hat{\boldsymbol{F}}_{i+\frac{1}{2},j,k}^{\mathrm{WENO}},\end{cases}\tag{3.7}$$

where the numerical flux $\hat{\boldsymbol{F}}_{i+\frac{1}{2},j,k}^{\mathrm{WENO}}$ is a high-order WENO scheme obtained by characterise-wise reconstruction (see Appendices A.1 and A.3). Next, calculate the corresponding density and pressure of $\boldsymbol{U}_{i,j,k}^{+}$ and $\boldsymbol{U}_{i+1,j,k}^{-}$. If either of them is negative or smaller than a prescribed value, then we reduce the order of the WENO scheme and recompute the WENO flux. In other words, the RFD criterion of ROR-WENO scheme is

$$\rho(\boldsymbol{U}_{i,j,k}^{+})\leq 0,\quad \rho(\boldsymbol{U}_{i+1,j,k}^{-})\leq 0,\quad p(\boldsymbol{U}_{i,j,k}^{+})\leq 0,\quad \text{or}\quad p(\boldsymbol{U}_{i+1,j,k}^{-})\leq 0.\tag{3.8}$$

This can be recursively performed until the 1st-order local Lax-Friedrichs (LLF) flux

$$\hat{\boldsymbol{F}}_{i+\frac{1}{2},j,k}^{\mathrm{LLF}}=\frac{1}{2}[\boldsymbol{F}_{i,j,k}+\boldsymbol{F}_{i+1,j,k}+\hat{\lambda}_s(\boldsymbol{U}_{i,j,k}^{n}-\boldsymbol{U}_{i+1,j,k}^{n})],\tag{3.9}$$

which has the positivity-preserving property under a proper CFL number. Here $\hat{\lambda}_s$ is given by (A.29) in Appendix A.3.

In general, the ROR procedure is activated only in extremely small portion of shock regions where the fluctuations are too strong, and hence should have only a negligible effect on the global formal order of the hybrid scheme but with significant improvement on its robustness. Another good property of this procedure is that it can be performed on an arbitrary single point, and thus would not consume too much extra computer time. Similar procedures can be applied to the flux $\boldsymbol{G}$ and $\boldsymbol{H}$, which are omitted here.

3.4 A positivity-preserving cooling function

The cooling function (3.4) is accomplished in program by directly changing the local internal energy per unit volume but keeping the local density and the average internal energy unchanged after cooling. Denote $E_0(\boldsymbol{x},t)$ and $E_1(\boldsymbol{x},t)$ as the internal-energy fields before and after cooling, respectively, there is

$$E_1(\boldsymbol{x},t)-E_0(\boldsymbol{x},t)=a(\boldsymbol{x},t)E_0(\boldsymbol{x},t)^b. \tag{3.10}$$

Note that we have replaced $T(\boldsymbol{x},t)$ in (3.4) by $E_0(\boldsymbol{x},t)$ since $E_0(\boldsymbol{x},t)$ is proportional to $T_0(\boldsymbol{x},t)$ and $\rho_0(\boldsymbol{x},t)$, and $\rho_0(\boldsymbol{x},t)$ can be absorbed into $a(\boldsymbol{x},t)$. Denote $\overline{E_0(\boldsymbol{x},t)}$ and $\overline{E_1(\boldsymbol{x},t)}$ as the spatial-averaged internal energies before and after cooling, respectively, of which the latter is assumed to be constant, $\overline{E_1(\boldsymbol{x},t)}=E=\text{const}$. Let b be the adjustable parameter, then from (3.10) there is

$$E_1(\boldsymbol{x},t)=E_0(\boldsymbol{x},t)+\frac{E-\overline{E_0(\boldsymbol{x},t)}}{\overline{E_0(\boldsymbol{x},t)^b}}E_0(\boldsymbol{x},t)^b. \tag{3.11}$$

Now it is clear when negative internal energy could happen: $\overline{E_0(\boldsymbol{x},t)}>E$, i.e., heat is removed from the system. In contrast, if $\overline{E_0(\boldsymbol{x},t)}<E$, i.e., heat is added into the system, then no negative internal energy would appear if $E_0(\boldsymbol{x},t)>0$.

It is very difficult (if not impossible) to determine all possible values of b such that $E_1(\boldsymbol{x},t)$ is positivity-preserving, i.e., $E_1(\boldsymbol{x},t)>0$ as long as $E_0(\boldsymbol{x},t)>0$. This is because that $E_0(\boldsymbol{x},t)$ can be regarded as a random field to some extent such that its operators of average and bth-order power can not be interchanged arbitrarily. Nevertheless, there are indeed some cases that they can be interchanged, say, $b=0$ and $b=1$. The former is the uniform cooling as adopted by Wang et al. [33], which indicates a translation of the reference internal energy. Since $E_0(\boldsymbol{x},t)$ may have very large fluctuations at very large M_t, this translation may lead some values of $E_0(\boldsymbol{x},t)$ falling below zero, resulting simulation blow-up. For the latter, (3.11) reduces to

$$E_1(\boldsymbol{x},t)=\frac{E}{\overline{E_0(\boldsymbol{x},t)}}E_0(\boldsymbol{x},t), \tag{3.12}$$

which means that the amount of heat removed or added is not a constant but a value proportional to the local internal energy and the inverse of averaged internal energy before cooling. Obviously, this operation is positivity-preserving and keeps the averaged

internal energy constant. Thus, we still adopt the cooling function (3.4), but propose the value of the parameter b to be 1 rather than 0 or 4 as [33] did.

We remark that although we have only proved that for $b=1$ the cooling function (3.11) is positivity-preserving, numerical results show that with proper initial conditions the instability phenomenon happens only for $b=0$, 3 and 4 but not for $b=1$ and 2. This fact enables us to study the effect of different cooling functions on the flow statistics of supersonic turbulence (see § 4.3 below).

4 Numerical results

In this section we consider some numerical simulations of stationary compressible isotropic turbulence at different resolutions and schemes, as well as different turbulent Mach numbers. The velocity field is always forced by fixing the total kinetic energy per unit mass in the first two wavenumber shells to $E(1)=1.242477$ and $E(2)=E(1)/2^{5/3}=0.391356$, and the forcing field is made incompressible. All simulations are performed by the 3rd-order Runge-Kutta method [57].

4.1 Dependence on the grid resolution

Three grid resolutions (128^3, 256^3 and 512^3) are considered in order to assess any dependence of small-scale flow statistics on the grid resolution. The initial conditions for turbulent Mach number $M_t=1.01$ are the random velocity field and uniform thermodynamic field, while for $M_t=2.05$ are the statistically stationary supersonic turbulence with a slightly smaller M_t. After reaching the stationary state, the time period about $10T_e$ is used to obtain statistically averages of interested quantities.

The flow statistics of the simulations are compiled in Table 1. The resolution parameters $k_{\max}\eta$ are, respectively, 1.4, 2.8 and 5.6 for $M_t=1.01$, where $k_{\max}$ is the maximum resolved wavenumber and η is the Kolmogorov length scale. Similar results can be obtained for the case $M_t=2.05$. The statistics shown in Table 1 imply that the small-scale flow is already well resolved in all these three resolutions. We note that in all these simulations the percentage of shock regions is about 10%, which deceases with the increasing

Table 1: Flow statistics of stationary compressible isotropic turbulence obtained by different resolutions.

Grid	M_t	R_λ	ε	η	L_I	T_e	$\vartheta_{\rm rms}$	$\omega_{\rm rms}$	S_3	WENO (%)
128^3	1.01	117	0.54	0.022	1.56	1.22	3.21	9.64	−0.77	10.8
256^3	1.01	112	0.58	0.021	1.55	1.21	3.73	9.82	−1.34	9.33
512^3	1.02	107	0.65	0.021	1.53	1.19	4.27	10.1	−2.25	7.94
128^3	2.06	128	0.39	0.022	1.69	1.40	4.65	6.79	−2.02	14.3
256^3	2.05	123	0.42	0.022	1.71	1.40	4.97	6.80	−3.15	13.5
512^3	2.04	117	0.48	0.021	1.69	1.39	5.43	7.07	−4.33	10.7

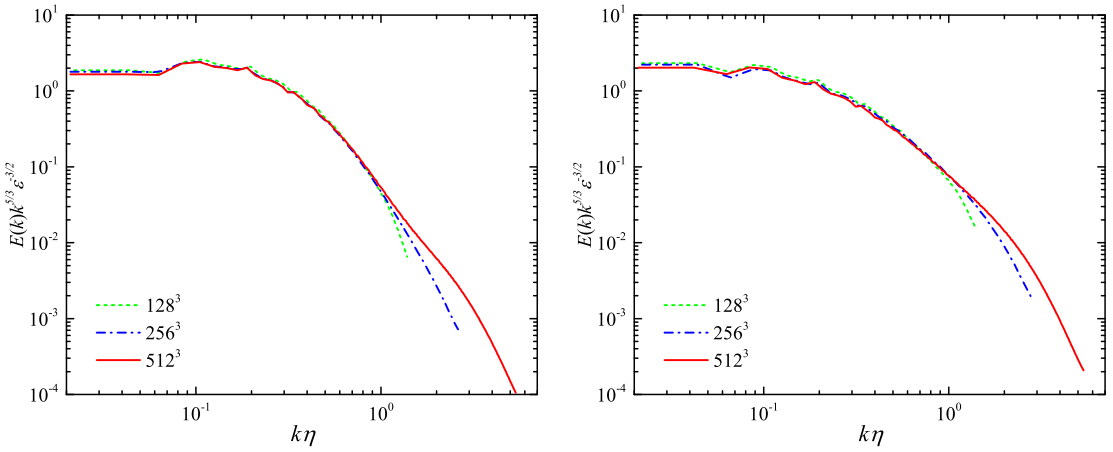

(a) $M_t=1.01$, $R_\lambda=112$ (b) $M_t=2.05$, $R_\lambda=123$

Figure 1: Grid convergence of averaged compensated kinetic energy spectra per unit mass of stationary compressible isotropic turbulence.

of grid resolution but increases with the increasing of M_t. On the other hand, the portion of ROR regions is even much smaller. For example, for $M_t=2.06$ with 128^3 resolution the percentage of spatial-temporal averaged ROR regions is as small as 1.27×10^{-6}. Thus, the ROR procedure should have a negligible effect on the formal order of the hybrid scheme.

In Fig. 1 we plot the averaged compensated kinetic energy spectra per unit mass for different grid resolutions and turbulent Mach numbers. All spectra tend to converge to that of 512^3 resolution. In particular, the energy spectra from 256^3 and 512^3 resolutions overlap in almost all resolved scale ranges, implying the convergence of energy spectra under this grid refinement. A very short inertial range is identified, with a Kolmogrov constant of about $E(1)\varepsilon^{-2/3}=2.0\pm0.3$. Evidently, this inertial range will extend when Reynolds number Re increases since η decreases with Re. In addition, the small-scale range for different M_t behaves very similarly, both having exponential decay tails. However, next to the exponential decay range, the spectrum decays more slowly for a larger M_t since the shocklets are stronger and happen more frequently, which can transfer the energy to smaller scales more easily.

In Fig. 2 we plot the probability density functions (PDFs) of normalized dilatation for different grid resolutions. The results show that the PDFs of 256^3 and 512^3 merge to each other very well, indicating again that the results are already convergent at the resolution of 256^3. Note that the PDFs of the dilatation in both flows have very long negative tails, which are the direct results of shocklets, the most significant flow structures of compressible turbulence. In particular, the proportion of negative tail of $M_t=2.05$ is larger than that of $M_t=1.01$, confirming that *shocklets appear more frequently in compressible turbulence with a larger turbulent Mach number*.

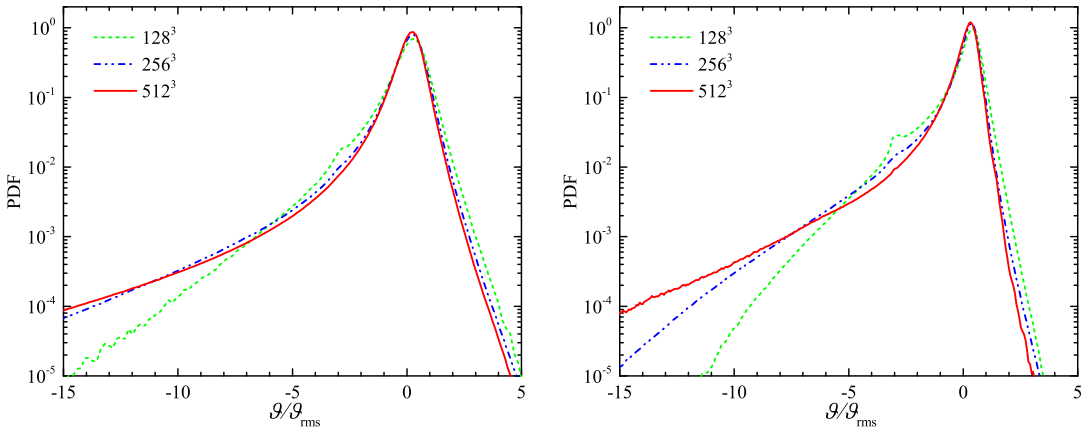

(a) $M_t=1.01$, $R_\lambda=112$ (b) $M_t=2.05$, $R_\lambda=123$

Figure 2: Grid convergence of PDFs of normalized dilatation $\vartheta/\vartheta_{\rm rms}$ of stationary compressible isotropic turbulence, where $\vartheta_{\rm rms}$ denotes the rms value of dilatation.

4.2 Comparison with Wang's scheme

Next we consider a few simulations for forced subsonic and nearly supersonic turbulence at 128^3 resolutions for both Wang's scheme and the present scheme (hereafter we call it Liu's scheme for short), where an identical initial flow is used and generated by Liu's scheme for about $10T_e$. The velocity field is forced by the same method described before, while a uniform cooling in space is adopted, namely, $b=0$ in (3.4). The total computation time is about $10T_e$, over which the statistical quantities are averaged.

The flow statistics of the simulations with different schemes are compiled in Table 2. Evidently, these statistic quantities are all consistent with each other perfectly, indicating the correctness of our scheme since the validation of Wang's scheme has been verified by comparing its result with that obtained by others (e.g., pseudo-spectral method and compact method [33]).

Table 2: Flow statistics of stationary compressible isotropic turbulence obtained by different schemes.

Scheme	M_t	R_λ	ε	η	L_I	T_e	$\vartheta_{\rm rms}$	$\omega_{\rm rms}$	S_3	WENO (%)
Wang	0.80	114	0.67	0.021	1.49	1.14	2.42	11.1	−0.51	8.67
Liu	0.80	114	0.68	0.021	1.48	1.13	2.55	11.2	−0.52	8.82
Wang	1.01	118	0.55	0.021	1.55	1.21	3.31	9.66	−0.81	10.9
Liu	1.02	116	0.55	0.021	1.55	1.21	3.41	9.69	−0.83	11.1

Fig. 3 compares the averaged compensated power spectra of velocity field at different turbulent Mach numbers obtained by Wang's and Liu's schemes. As we expected, there is no distinguishable difference between the results obtained by these two schemes. For other quantities, for example, the PDFs of longitudinal velocity increment $\Delta u(r)=[\boldsymbol{u}(\boldsymbol{x}+$

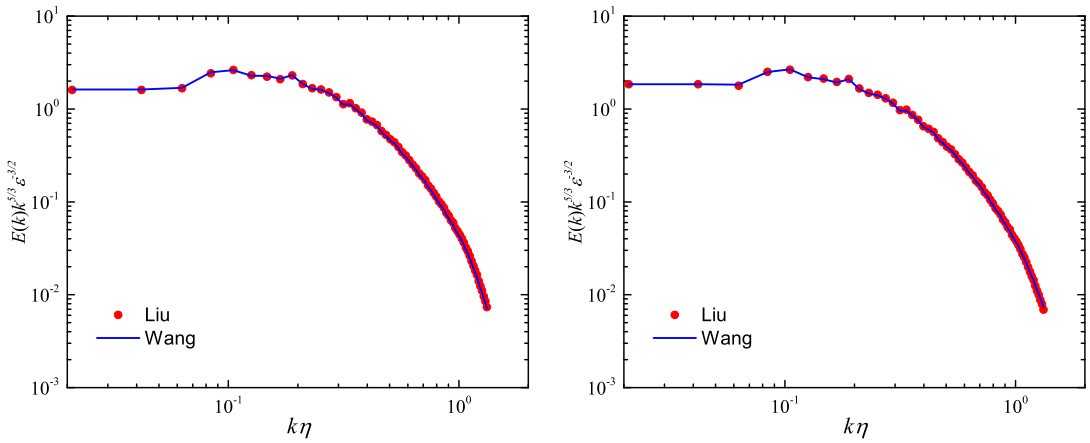

(a) $M_t=0.80$, $R_\lambda=114$ (b) $M_t=1.02$, $R_\lambda=116$

Figure 3: Comparison of averaged compensated spectra of velocity field in stationary compressible isotropic turbulence, simulated with 128^3 grid resolution.

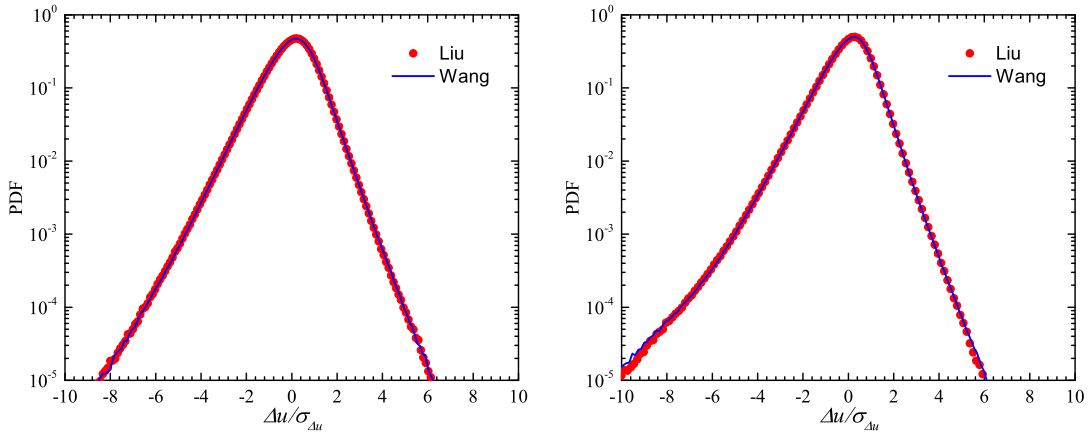

(a) $M_t=0.80$, $R_\lambda=114$ (b) $M_t=1.02$, $R_\lambda=116$

Figure 4: Comparison of averaged PDFs of longitudinal velocity increment at a separation equals to Δx of stationary compressible isotropic turbulence, simulated with 128^3 grid resolution, where $\sigma_{\Delta u}$ denotes the standard deviation of Δu.

$\boldsymbol{r})-\boldsymbol{u}(\boldsymbol{x})]\cdot\boldsymbol{r}/r$ and local density as shown in Figs. 4 and 5, respectively, the results are also consistent with each other, and only very slightly differences exist at the tails, where the number of sample points are too small to obtain reliable results. Therefore, the good properties of Wang's scheme have indeed been inherited by Liu's scheme. Note that, in order to display the PDF tails more clearly, the logarithmic coordinate has been used.

In the remaining of this paper, some numerical results of supersonic isotropic turbulence with turbulent Mach number greater than but not close to unity are presented.

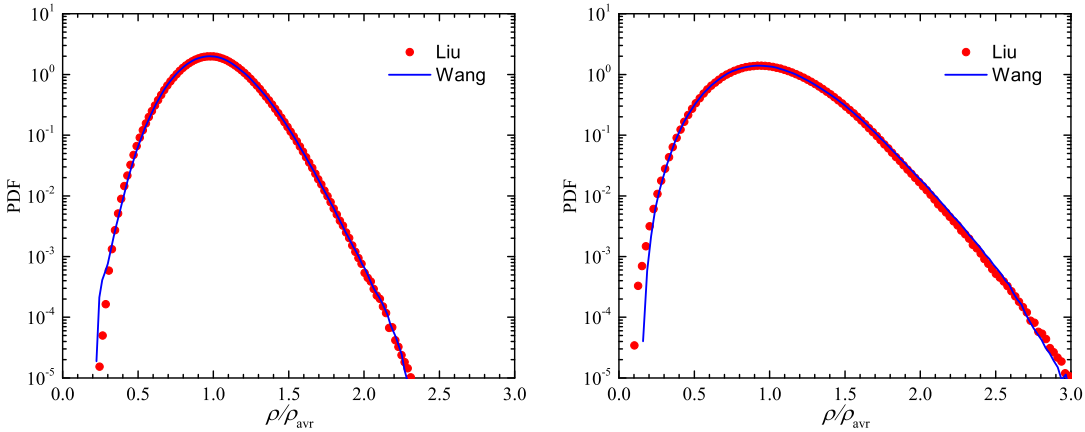

(a) $M_t = 0.80$, $R_\lambda = 114$ (b) $M_t = 1.02$, $R_\lambda = 116$

Figure 5: Comparison of averaged PDFs of local density of stationary compressible isotropic turbulence, simulated with 128^3 grid resolution, where ρ_{avr} denotes the averaged density.

These results can only be obtained by the present scheme but not the original hybrid scheme since the latter will blow-up at such a high turbulent Mach number. To our knowledge, this is also the first time that such a high turbulent Mach number ever simulated in the framework of compressible Navier-Stokes equations.

4.3 Effect of different cooling functions

Now we consider a few simulations of forced supersonic turbulence at 256^3 resolutions with different b in the cooling function (3.11). At this turbulent Mach number regime and grid resolution, the runs with $b = 0$, 3 and 4 were observed to blow-up. Therefore, the results of two runs corresponding to the cooling function with $b = 1$ and 2 are presented here. An identical initial flow is used and generated by the run $b = 1$ for about $10T_e$. The time is then reset to zero and the different cooling functions are applied to generate the corresponding results. The flow statistics of the simulations with different cooling functions are compiled in Table 3. Evidently, there are only very slightly differences between these two results.

Table 3: Flow statistics of stationary compressible isotropic turbulence obtained by different cooling functions.

b	M_t	R_λ	ε	η	L_I	T_e	ϑ_{rms}	ω_{rms}	S_3	WENO (%)
1	2.05	123	0.42	0.022	1.71	1.40	4.97	6.80	−3.15	13.5
2	2.01	124	0.41	0.022	1.71	1.39	4.64	6.91	−2.94	13.2

Fig. 6 compares the time evolution of space-averaged longitudinal velocity derivative skewness S_3 and the dilatation ϑ_{rms}. The average S_3 for the two runs are −3.15 and −2.94,

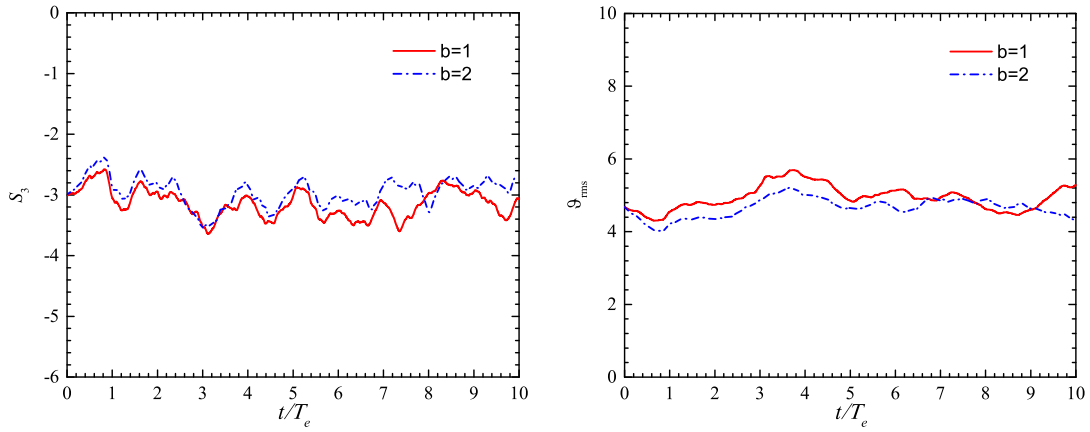

(a) Skewness (b) Dilatation

Figure 6: Evolution of (a) longitudinal velocity derivative skewness and (b) dilatation for the forced supersonic turbulence with $M_t=2.05$ and $R_\lambda=123$, simulated with 256^3 grid resolution but different cooling functions.

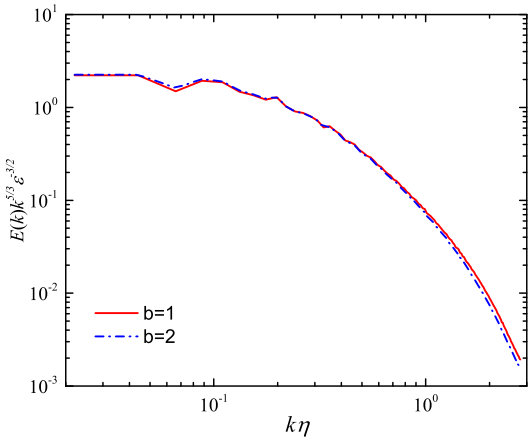

Figure 7: Averaged kinetic energy spectra per unit mass of the forced supersonic turbulence with $M_t=2.05$ and $R_\lambda=123$, simulated with 256^3 grid resolution but different cooling functions

respectively. Such a large magnitude of S_3 is not possible for incompressible turbulence, and results from very strong compression across the shocklets. In particular, the stronger the non-uniformity in the cooling rate (i.e., the larger b), the weaker the jumps across the shocklets as indicated by the somewhat smaller magnitudes in dilatation and skewness (similar results in subsonic isotropic turbulence has also been obtained by Wang et al. [33]). Nevertheless, the kinetic energy spectra per unit mass obtained by different cooling functions are almost identical (see Fig. 7), indicating that the flow statistics are not very sensitive to the exact form of the cooling function used.

4.4 Preliminary study of supersonic isotropic turbulence

Finally, we give a preliminary study about the statistics of supersonic isotropic turbulence at turbulent Mach number $M_t=2.08$ and Taylor-microscale Reynolds number $R_\lambda=200$, using 512^3 grid resolution and the cooling function (3.11) with $b=1$. The main flow statistics are complied in Table 4.

Table 4: Flow statistics of stationary supersonic isotropic turbulence.

Grid	M_t	R_λ	ε	η	L_I	T_e	$\vartheta_{\rm rms}$	$\omega_{\rm rms}$	S_3	WENO (%)
512^3	2.08	200	0.40	0.013	1.63	1.31	7.91	10.3	-4.06	11.3

Before proceeding, we introduce the well-known Helmholtz decomposition, which can split the total velocity $\boldsymbol{u}$ into a solenoidal part and a compressive part, namely,

$$\boldsymbol{u}=\boldsymbol{u}^c+\boldsymbol{u}^s=\nabla\phi+\nabla\times\boldsymbol{\psi},\quad \nabla\cdot\boldsymbol{\psi}=0, \tag{4.1}$$

where $\boldsymbol{u}^c=\nabla\phi$ is the compressive velocity and $\boldsymbol{u}^s=\nabla\times\boldsymbol{\psi}$ is the solenoidal velocity. Therefore, the corresponding spectrum of velocity field can also be split into a solenoidal part and a compressive part, i.e.,

$$E(k)=E^s(k)+E^c(k), \tag{4.2}$$

where

$$\frac{1}{2}\langle\boldsymbol{u}^s\cdot\boldsymbol{u}^s\rangle=\int_0^\infty E^s(k)\mathrm{d}k,\quad \frac{1}{2}\langle\boldsymbol{u}^c\cdot\boldsymbol{u}^c\rangle=\int_0^\infty E^c(k)\mathrm{d}k. \tag{4.3}$$

Because this decomposition does not rely on any assumption dealing with the amplitude of the turbulent fluctuations, it is a very useful tool to handle flows in which nonlinear mechanisms are dominant. Finally, we rewrite the dissipation (2.18) as

$$\langle\varepsilon\rangle=\langle\varepsilon_c\rangle+\langle\varepsilon_s\rangle-\langle 2\mu\nabla\cdot(\mathbf{B}\cdot\boldsymbol{u})\rangle, \tag{4.4}$$

where $\varepsilon_c\equiv\mu_\theta\vartheta^2$ and $\varepsilon_s\equiv\mu\omega^2$ are called compressive and solenoidal dissipations, respectively, and the last term is usually negligible. Actually, our numerical results show that $\langle\varepsilon\rangle=0.584$, $\langle\varepsilon_c\rangle=0.092$ and $\langle\varepsilon_s\rangle=0.486$ when $M_t=1.01$ and $R_\lambda=107$, while $\langle\varepsilon\rangle=0.420$, $\langle\varepsilon_c\rangle=0.174$ and $\langle\varepsilon_s\rangle=0.244$ when $M_t=2.05$ and $R_\lambda=123$. In all these two cases the ratio of the last term over the total dissipation is no more than 1%.

Fig. 8(a) shows the normalized PDFs of longitudinal velocity increments, $\Delta u^s(r)=\Delta\boldsymbol{u}^s(\boldsymbol{r})\cdot\boldsymbol{r}/r$, of the solenoidal component at different separations, where $\boldsymbol{r}$ is the separation vector and $r=|\boldsymbol{r}|$. The PDFs exhibit stretched exponential tails at small spatial separations and approach Gaussian as the separation increases. Fig. 8(b) shows the normalized PDFs of the longitudinal velocity increments, $\Delta u^c(r)=\Delta\boldsymbol{u}^c(\boldsymbol{r})\cdot\boldsymbol{r}/r$, of the compressive component. The shapes of the PDFs are highly skewed at small separations but also tends to Gaussian as the separation increases. These trends are very similar to those found in subsonic isotropic turbulence [67], where the skewnesses of solenoidal velocity and compressive velocity are attributed to the vortex filaments and shocklets,

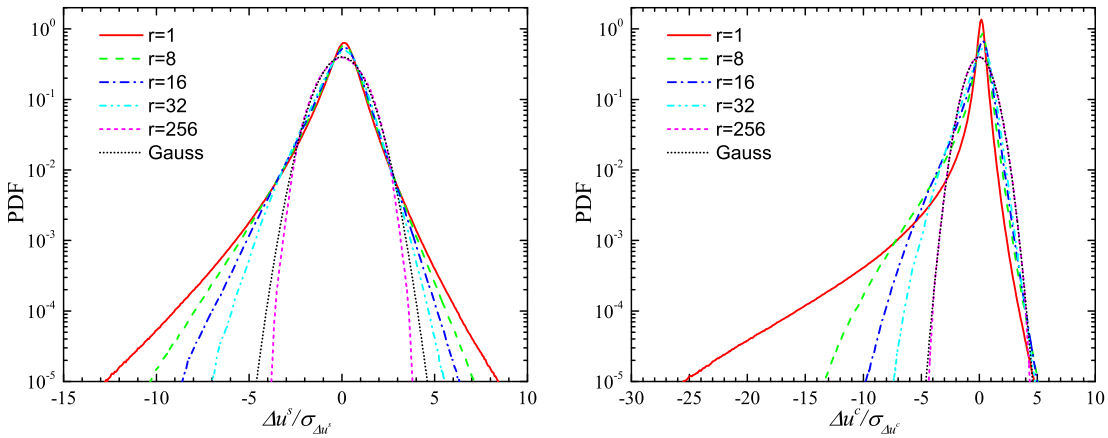

(a) Solenoidal velocity (b) Compressive velocity

Figure 8: Normalized PDFs of longitudinal velocity increments at separations equal to $r\Delta x$ of stationary supersonic turbulence with $M_t = 2.08$ and $R_\lambda = 200$, simulated with 512^3 grid resolution. Here $\sigma_{\Delta u}$ is the standard deviation of Δu. (a) Solenoidal velocity increments Δu^s; (b) compressive velocity increments Δu^c.

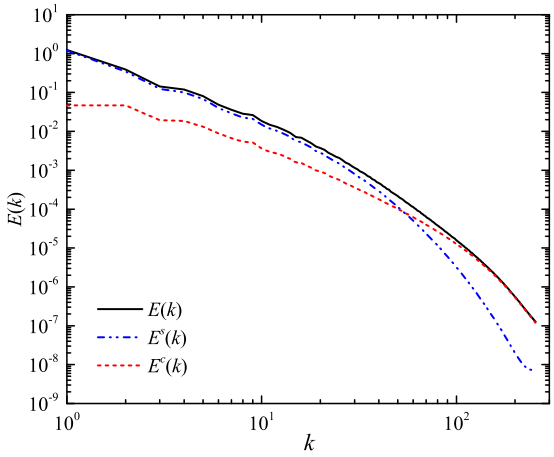

Figure 9: Spectra for kinetic energy per unit mass and its solenoidal and compressive components of stationary supersonic turbulence with $M_t = 2.08$ and $R_\lambda = 200$, simulated with 512^3 grid resolution.

respectively. Since the skewness magnitude of compressive velocity is much larger than that of the solenoidal velocity, it is supposed that the shocklets can strongly strengthen the intermittency of turbulence. In addition, the corresponding spectra for kinetic energy per unit mass and its solenoidal and compressive components are shown in Fig. 9, where at large scales the solenoidal spectrum holds a dominant role, while at small scales the compressive spectrum overrides the former.

Fig. 10 shows the normalized PDFs of pressure increments at different separations. In sharp contrast to the subsonic turbulence [68], the shapes of the PDFs deviate Gaussian

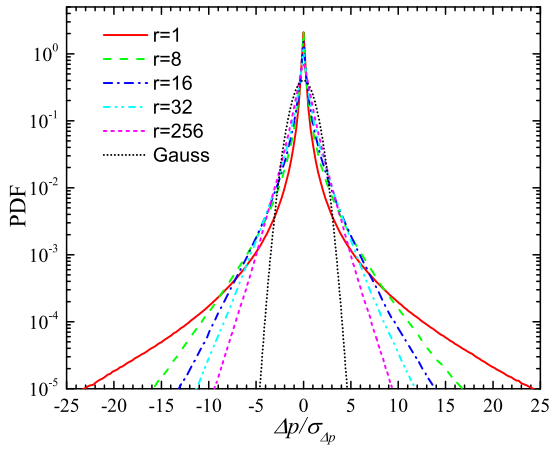

Figure 10: Normalized PDFs of pressure increments at separations equal to $r\Delta x$ of stationary supersonic turbulence with $M_t=2.08$ and $R_\lambda=200$, simulated with 512^3 grid resolution. Here $\sigma_{\Delta p}$ is the standard deviation of pressure increment Δp.

significantly even for the largest possible separation. This is an indication that the thermodynamic process will take a very important role in the dynamics of turbulence, such as the energy transfer between the internal energy and kinetic energy. Actually, our numerical results show that $\langle p\vartheta\rangle=-0.021$ when $M_t=1.01$ and $R_\lambda=107$, while $\langle p\vartheta\rangle=-0.174$ when $M_t=2.05$ and $R_\lambda=123$ or $\langle p\vartheta\rangle=-0.204$ when $M_t=2.08$ and $R_\lambda=200$. This huge increment in the magnitude of $\langle p\vartheta\rangle$ is an indication of strong coupling among various dynamic processes.

Fig. 11(a) shows the instantaneous contour of vortices. Like incompressible turbulence, the main structures of solenoidal field are tubulike surfaces, which are obtained by the iso-surface of Q-criteria with $Q=30$. In comparison, Fig. 11(b) shows the instantaneous contour of shocklets. The shocklets contour is obtained by the iso-surface of dilatation field with $\vartheta/\vartheta_{\rm rms}=-3$, in which the main structures are sheetlike surfaces. This is in consistent with the fact that shocklets are very small shocks that form when turbulent eddies allow for the local steepening of pressure waves [45]. Therefore they should have all the characteristics of a typical shock wave, such as proper jumps in pressure and density along with a local entropy peak inside the high-compression zone [46].

A direct consequence of more and stronger shocklets is that the thermodynamic quantities have much larger fluctuations, which means that very small, as well as very large, density and pressure could appear. To see this conclusion more clearly, Fig. 12 shows the instantaneous contours of logarithmic values of density and pressure on the same slice. Note that the contours of density and pressure are very similar with each other, although significant differences indeed exist especially in strong shock regions. Nevertheless, we found that the ratio of the largest density or pressure over the smallest density or pressure is larger than hundreds. It is the appearance of such large fluctuations of thermodynamic quantities that may lead the numerical simulation to blow-up.

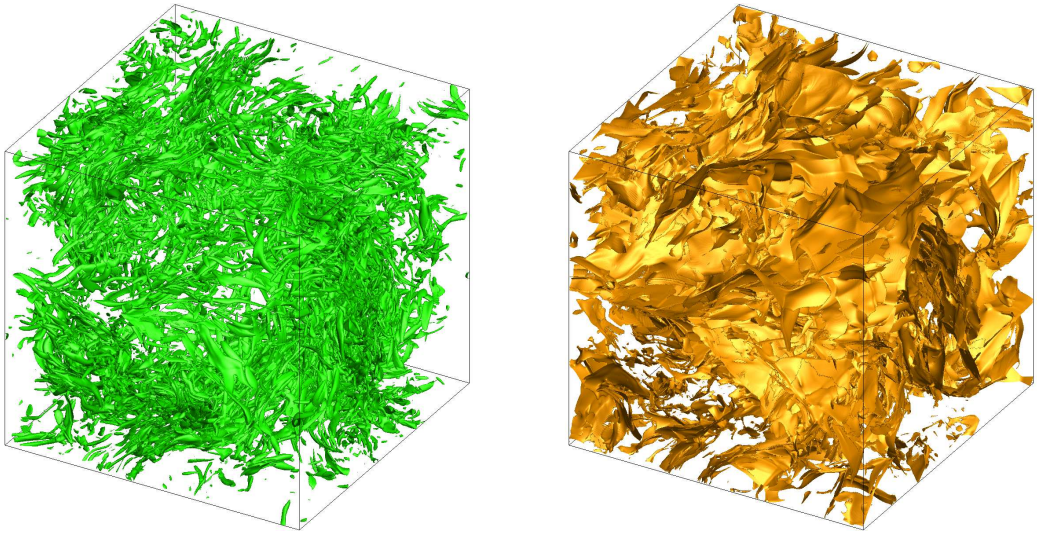

(a) Vortices (b) Shocklets

Figure 11: Instantaneous contours of vortices (a) and shocklets (b) of stationary supersonic isotropic turbulence with $M_t=2.08$ and $R_\lambda=200$, simulated with 512^3 grid resolution. Note that the tubelike vortices are the iso-surface of Q-criteria with $Q=30$, while the sheetlike shocklets are the iso-surface of dilatation field with $\vartheta/\vartheta_{\rm rms}=-3$.

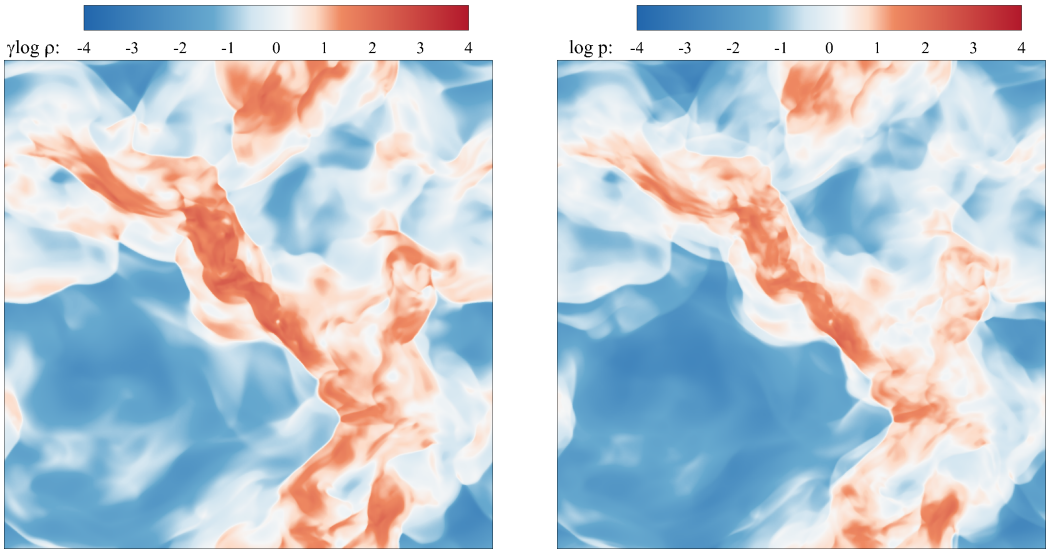

(a) Density (b) Pressure

Figure 12: Instantaneous contours of density (a) and pressure (b) on the same slice of stationary supersonic isotropic turbulence with $M_t=2.08$ and $R_\lambda=200$, simulated with 512^3 grid resolution.

5 Conclusions

In this paper, the hybrid scheme proposed by [33] has been extended to the simulation of supersonic isotropic turbulence with turbulent Mach number greater than unity. To achieve this goal, some techniques have been utilized. Firstly, in order to reduce non-physical oscillations, the original hybrid scheme has been modified to the conservation form and the characteristic-wise reconstruction has been adopted. The latter is necessary to obtain a monotonic flux. Secondly, the recursive-order-reduction (ROR) method has been applied to the WENO sub-scheme, where a positivity-preserving reconstruction-failure-detection criterion is constructed. This sub-scheme is very effective to capture shocklets/shocks with sufficient resolution and accuracy. Finally, a new cooling function has been proposed, which has been further proved also to be positivity-preserving. The validation and effectiveness of the new scheme has been verified by numerical simulations of compressible isotropic turbulence with different grid resolutions, different schemes, and different turbulent Mach numbers.

With the present scheme, one can obtain numerical data of supersonic turbulence of viscous fluid and make detailed flow analyses, which can help us to understand the compressible turbulence in supersonic regime.

Acknowledgments

This work was supported by National Natural Science Foundation of China (Grant Nos. 11702127, 11521091, 91752202) and Science Challenge Project (No. TZ2016001). The numerical computation was partially performed on TianHe-1(A) at the National Supercomputer Center in Guangzhou. The authors are very grateful to the anonymous referees for their helpful comments, which improved an early version of this paper. The authors also want to appreciate the valuable comments of Profs. Yan-Tao Yang, Zuo-Li Xiao and Xin-Liang Li. The first author gratefully acknowledges the support of Boya Postdoctoral Fellowship.

Appendix

A Some details involved in the present hybrid scheme

A.1 The 7th-order WENO scheme

Consider the scalar hyperbolic conservation law given by

$$\frac{\partial u}{\partial t}+\frac{\partial f(u)}{\partial x}=0. \tag{A.1}$$

Let $\{I_j\}$ be a uniform grid, where $I_j=\{x_{j-1/2}, x_{j+1/2}\}$ and $x_{j+1/2}-x_{j-1/2}=\Delta x$. The semi-discrete conservative finite difference scheme of (A.1) can be written as

$$\frac{\partial u}{\partial t}+\frac{\hat{f}_{j+1/2}-\hat{f}_{j-1/2}}{\Delta x}=0, \tag{A.2}$$

where $\hat{f}_{j+1/2}$ is the numerical flux function.

For the 7th-order WENO scheme, $\hat{f}_{j+1/2}$ can be reconstructed as [54]

$$\hat{f}_{j+1/2}=\sum_{k=0}^{3}\omega_k q_k(x_{j+1/2};f_{j+k-3},\cdots,f_{j+k}), \tag{A.3}$$

where

$$\begin{cases} q_0(x_{j+1/2})=\dfrac{1}{12}(-3f_{j-3}+13f_{j-2}-23f_{j-1}+25f_j), \\ q_1(x_{j+1/2})=\dfrac{1}{12}(f_{j-2}-5f_{j-1}+13f_j+3f_{j+1}), \\ q_2(x_{j+1/2})=\dfrac{1}{12}(-f_{j-1}+7f_j+7f_{j+1}-f_{j+2}), \\ q_3(x_{j+1/2})=\dfrac{1}{12}(3f_j+13f_{j+1}-5f_{j+2}+f_{j+3}), \end{cases} \tag{A.4}$$

and

$$\omega_k=\frac{\alpha_k}{\sum_{n=0}^{3}\alpha_n},\quad \alpha_k=\frac{C_k}{(\epsilon+\mathrm{IS}_k)^p}. \tag{A.5}$$

Here,

$$p=2,\quad \epsilon=10^{-6},\quad C_0=\frac{1}{35},\quad C_1=\frac{12}{35},\quad C_2=\frac{18}{35},\quad C_3=\frac{4}{35}, \tag{A.6}$$

and

$$\mathrm{IS}_k=\left[q_k^{(1)}(x_j)\right]^2+\frac{13}{12}\left[q_k^{(2)}(x_j)\right]^2+\frac{1043}{960}\left[q_k^{(3)}(x_j)\right]^2+\frac{1}{12}q_k^{(1)}(x_j)q_k^{(3)}(x_j), \tag{A.7}$$

where $k=0,1,2,3$ and

$$\begin{cases} q_0^{(1)}(x_j)=\dfrac{1}{6}(-2f_{j-3}+9f_{j-2}-18f_{j-1}+11f_j), \\ q_1^{(1)}(x_j)=\dfrac{1}{6}(f_{j-2}-6f_{j-1}+3f_j+2f_{j+1}), \\ q_2^{(1)}(x_j)=\dfrac{1}{6}(-2f_{j-1}-3f_j+6f_{j+1}-f_{j+2}), \\ q_3^{(1)}(x_j)=\dfrac{1}{6}(-11f_j+18f_{j+1}-9f_{j+2}+2f_{j+3}), \end{cases} \tag{A.8}$$

$$\begin{cases} q_0^{(2)}(x_j) = -f_{j-3} + 4f_{j-2} - 5f_{j-1} + 2f_j, \\ q_1^{(2)}(x_j) = f_{j-1} - 2f_j + f_{j+1}, \\ q_2^{(2)}(x_j) = f_j - 2f_{j+1} + f_{j+2}, \\ q_3^{(2)}(x_j) = 2f_j - 5f_{j+1} + 4f_{j+2} - f_{j+3}, \end{cases} \tag{A.9}$$

$$\begin{cases} q_0^{(3)}(x_j) = -f_{j-3} + 3f_{j-2} - 3f_{j-1} + f_j, \\ q_1^{(3)}(x_j) = -f_{j-2} + 3f_{j-1} - 3f_j + f_{j+1}, \\ q_2^{(3)}(x_j) = -f_{j-1} + 3f_j - 3f_{j+1} + f_{j+2}, \\ q_3^{(3)}(x_j) = -f_j + 3f_{j+1} - 3f_{j+2} + f_{j+3}. \end{cases} \tag{A.10}$$

We remark that the above arguments are only suitable for positive flux. Nevertheless, the negative flux is the same as the positive one but with $j+k$ replaced by $j+1-k$.

A.2 The 8th-order compact scheme with built-in hyperviscosity

The compact schemes were first proposed by Lele [55], of which the 8th-order approximation of the 1st-order spatial derivative in (A.1) can be expressed as

$$\alpha_1 f'_{j-1} + f'_j + \alpha_1 f'_{j+1} = a_1 \frac{f_{j+1} - f_{j-1}}{\Delta x} + b_1 \frac{f_{j+2} - f_{j-2}}{\Delta x} + c_1 \frac{f_{j+3} - f_{j-3}}{\Delta x}, \tag{A.11}$$

where Δx is the grid spacing and

$$\alpha_1 = \frac{3}{8}, \quad a_1 = \frac{25}{32}, \quad b_1 = \frac{1}{20}, \quad c_1 = -\frac{1}{480}. \tag{A.12}$$

Since the central schemes are not stable due to the existence of alias error [69], a natural numerical viscosity treatment called hyperviscosity has been proposed by Wang et al. [33]. In practice, it is simply implemented as

$$\frac{\partial u}{\partial t} = \nu_n [u''_n - (u'_n)'_n], \tag{A.13}$$

where u is the primary variable, ν_n is the hyperviscosity coefficient, the subscript n denotes numerical approximation, and the prime $'$ denotes spatial derivative. The first term in the right-hand side of (A.13) is accomplished by applying the 8th-order compact scheme directly to the 2nd-order derivative,

$$\beta_3 u''_{j-2} + \alpha_3 u''_{j-1} + u''_j + \alpha_3 u''_{j+1} + \beta_3 u''_{j+2} = a_3 \frac{u_{j+1} - 2u_j + u_{j-1}}{\Delta x^2} + b_3 \frac{u_{j+2} - 2u_j + u_{j-2}}{\Delta x^2}, \tag{A.14}$$

where

$$\alpha_3 = \frac{344}{1179}, \quad \beta_3 = \frac{23}{2358}, \quad a_3 = \frac{320}{393}, \quad b_3 = \frac{155}{786}. \tag{A.15}$$

In contrast, the second term is computed by applying the 8th-order compact scheme twice to the 1st-order derivative but with the same stencil width,

$$\beta_2 u'_{j-2}+\alpha_2 u'_{j-1}+u'_j+\alpha_2 u'_{j+1}+\beta_2 u'_{j+2}=a_2\frac{u_{j+1}-u_{j-1}}{\Delta x}+b_2\frac{u_{j+2}-u_{j-2}}{\Delta x}, \tag{A.16}$$

where

$$\alpha_2=\frac{4}{9},\quad \beta_2=\frac{1}{36},\quad a_2=\frac{20}{27},\quad b_2=\frac{25}{216}. \tag{A.17}$$

For better numerical stability, the first term u''_n in (A.13) is handled by the implicit Euler scheme, while the second term $-(u'_n)'_n$ is time-advanced by an explicit Euler scheme.

A.3 Characteristic-wise reconstruction

Consider the vector hyperbolic conservation law given by [32]

$$\frac{\partial \boldsymbol{U}}{\partial t}+\frac{\partial \boldsymbol{F}(\boldsymbol{U})}{\partial x}+\frac{\partial \boldsymbol{G}(\boldsymbol{U})}{\partial y}+\frac{\partial \boldsymbol{H}(\boldsymbol{U})}{\partial z}=\boldsymbol{0}, \tag{A.18}$$

where

$$\boldsymbol{U}=\begin{pmatrix}\rho\\ \rho u\\ \rho v\\ \rho w\\ E\end{pmatrix},\quad \boldsymbol{F}=\begin{pmatrix}\rho u\\ \rho u^2+p\\ \rho uv\\ \rho uw\\ u(E+p)\end{pmatrix},\quad \boldsymbol{G}=\begin{pmatrix}\rho v\\ \rho vu\\ \rho v^2+p\\ \rho vw\\ v(E+p)\end{pmatrix},\quad \boldsymbol{H}=\begin{pmatrix}\rho w\\ \rho wu\\ \rho wv\\ \rho w^2+p\\ w(E+p)\end{pmatrix}. \tag{A.19}$$

To illustrate the idea of characteristic-wise reconstruction, we take $\boldsymbol{F}$ as an example.

First, define

$$H=k+\frac{a^2}{\hat{\gamma}},\quad k=\frac{1}{2}(u^2+v^2+w^2),\quad a=\sqrt{\frac{\gamma p}{\rho}},\quad \hat{\gamma}=\gamma-1. \tag{A.20}$$

Then we have [16]

$$\mathbf{A}\equiv\frac{\partial \boldsymbol{F}}{\partial \boldsymbol{U}}=\begin{pmatrix}0 & 1 & 0 & 0 & 0\\ \hat{\gamma}k-u^2 & (3-\gamma)u & -\hat{\gamma}v & -\hat{\gamma}w & \hat{\gamma}\\ -uv & v & u & 0 & 0\\ -uw & w & 0 & u & 0\\ (\hat{\gamma}k-H)u & H-\hat{\gamma}u^2 & -\hat{\gamma}uv & -\hat{\gamma}uw & \gamma u\end{pmatrix}, \tag{A.21}$$

of which the eigenvalues are

$$\lambda_1^A=u-a,\quad \lambda_{2,3,4}^A=u,\quad \lambda_5^A=u+a, \tag{A.22}$$

and the corresponding right and left eigenvectors are

$$\mathbf{R}_A=\begin{pmatrix} 1 & 1 & 0 & 0 & 1 \\ u-a & u & 0 & 0 & u+a \\ v & v & 1 & 0 & v \\ w & w & 0 & 1 & w \\ H-ua & k & v & w & H+ua \end{pmatrix}, \tag{A.23}$$

$$\mathbf{L}_A=\frac{\hat{\gamma}}{2a^2}\begin{pmatrix} k+\frac{a}{\hat{\gamma}}u & -u-\frac{a}{\hat{\gamma}} & -v & -w & 1 \\ \frac{2a^2}{\hat{\gamma}}-2k & 2u & 2v & 2w & -2 \\ -\frac{2a^2}{\hat{\gamma}}v & 0 & \frac{2a^2}{\hat{\gamma}} & 0 & 0 \\ -\frac{2a^2}{\hat{\gamma}}w & 0 & 0 & \frac{2a^2}{\hat{\gamma}} & 0 \\ k-\frac{a}{\hat{\gamma}}u & -u+\frac{a}{\hat{\gamma}} & -v & -w & 1 \end{pmatrix}. \tag{A.24}$$

Next, we adopt the local characteristic decompositions,

$$\mathbf{A}_{j+1/2}=\left.\frac{\partial \boldsymbol{F}(\boldsymbol{U})}{\partial \boldsymbol{U}}\right|_{j+1/2}, \tag{A.25}$$

where $\boldsymbol{U}_{j+1/2}$ is the Roe average [70],

$$\begin{cases} u_{j+1/2}=\dfrac{\sqrt{\rho_j}u_j+\sqrt{\rho_{j+1}}u_{j+1}}{\sqrt{\rho_j}+\sqrt{\rho_{j+1}}}, \quad v_{j+1/2}=\dfrac{\sqrt{\rho_j}v_j+\sqrt{\rho_{j+1}}v_{j+1}}{\sqrt{\rho_j}+\sqrt{\rho_{j+1}}}, \\ w_{j+1/2}=\dfrac{\sqrt{\rho_j}w_j+\sqrt{\rho_{j+1}}w_{j+1}}{\sqrt{\rho_j}+\sqrt{\rho_{j+1}}}, \quad H_{j+1/2}=\dfrac{\sqrt{\rho_j}H_j+\sqrt{\rho_{j+1}}H_{j+1}}{\sqrt{\rho_j}+\sqrt{\rho_{j+1}}}, \\ a_{j+1/2}=\sqrt{(\gamma-1)\left[H_{j+1/2}-\dfrac{1}{2}\left(u_{j+1/2}^2+v_{j+1/2}^2+w_{j+1/2}^2\right)\right]}. \end{cases} \tag{A.26}$$

Then, by projecting the fluxes onto the characteristic plane, there is

$$F_{s;j+k}^{\pm}=\frac{1}{2}\boldsymbol{l}_{s,j+1/2}\cdot\boldsymbol{F}_{j+k}^{\pm}, \quad s=1,\cdots,5, \tag{A.27}$$

where the local Lax-Friedrichs flux is used as the building blocks,

$$\boldsymbol{F}=\boldsymbol{F}^{+}+\boldsymbol{F}^{-}, \quad \boldsymbol{F}^{\pm}=\frac{1}{2}(\boldsymbol{F}\pm\hat{\lambda}_s\boldsymbol{U}), \tag{A.28}$$

and

$$\hat{\lambda}_s=\chi\max(|\lambda_{s;j+1/2}|,\,|\lambda_{s;j-r+1}|,\,\cdots,\,|\lambda_{s;j+r-1}|), \quad s=1,\cdots,5. \tag{A.29}$$

Here, $\chi=1.2$ is adopted to control the amount of dissipation introduced into the numerical scheme, λ_s is given by (A.22), and $2r-1$ is the order of the WENO scheme.

Applying the $(2r-1)$th-order scalar WENO scheme to each of the characteristic field, we have for the s-th field of positive flux,

$$\hat{F}^{+}_{s,j+1/2}=\sum_{k=0}^{r-1}\omega_{s,k}q_k(F^{+}_{s,j+k-2},F^{+}_{s,j+k-1},F^{+}_{s,j+k}), \tag{A.30}$$

$$\hat{F}^{-}_{s,j+1/2}=\sum_{k=0}^{r-1}\omega_{s,k}q_k(F^{-}_{s,j-k-1},F^{-}_{s,j-k},F^{-}_{s,j-k+1}). \tag{A.31}$$

Details about this reconstruction with $r=4$ can be found in Appendix A.1.

Finally, the numerical fluxes obtained in each characteristic field can then be projected back to the physical space by

$$\hat{\boldsymbol{F}}_{j+1/2}=\sum_{s=1}^{5}(\hat{F}^{+}_{s,j+1/2}+\hat{F}^{-}_{s,j+1/2})\boldsymbol{r}_{s,j+1/2}. \tag{A.32}$$

Similar procedures can be similarly applied to the fluxes $\boldsymbol{G}$ and $\boldsymbol{H}$.

References

[1] B. G. Elmegreen, J. Scalo, Interstellar turbulence I: Observations and processes, Annu. Rev. Astron. Astrophys. 42 (2004) 211–273.

[2] J. Scalo, B. G. Elmegreen, Interstellar turbulence II: Implications and effects, Annu. Rev. Astron. Astrophys. 42 (2004) 275–316.

[3] O. Alexandrova, C. H. K. Chen, L. Sorriso-Valvo, T. S. Horbury, S. D. Bale, Solar wind turbulence and the role of ion instabilities, Space Sci. Rev. 178 (2013) 101–139.

[4] C. F. Mckee, E. C. Ostriker, Theory of star formation, Annu. Rev. Astron. Astrophys. 45 (2007) 565–687.

[5] S. B. Pope, Computations of turbulent combustion: Progress and challenges, Symposium on Combustion 23 (1991) 591–612.

[6] A. Ingenito, C. Bruno, Physics and regimes of supersonic combustion, AIAA J. 48 (2010) 515–525.

[7] J. D. Lindl, Inertial Confinement Fusion: The Quest for Ignition and Energy Gain Using Indirect Drive, Springer, New York, 1998.

[8] X. T. He, J. W. Li, Z. F. Fan, L. F. Wang, J. Liu, K. Lan, J. F. Wu, W. H. Ye, A hybrid-drive nonisobaric-ignition scheme for inertial confinement fusion, Phys. Plasmas 23 (2016) 082706.

[9] S. A. Orszag, G. S. Patterson, Numerical simulation of three-dimensional homogeneous isotropic turbulence, Phys. Rev. Lett. 28 (1972) 76–79.

[10] E. Hewitt, R. E. Hewitt, The Gibbs-Wilbraham phenomenon: An episode in Fourier analysis, Archive for History of Exact Sciences 21 (1979) 129–160.

[11] G. Moretti, Computation of flows with shocks, Annu. Rev. Fluid Mech. 19 (1987) 313–337.

[12] J. Von Neumann, R. D. Richtmyer, A method for the numerical calculation of hydrodynamic shocks, J. Appl. Phys. 21 (1950) 232–237.

[13] S. K. Godunov, A difference scheme for numerical computation of discontinuous solution of hydrodynamic equations, Rossiiskaya Akademiya Nauk. Matematicheskii Sbornik 47 (1959) 271–306.

[14] B. van Leer, Towards the ultimate conservative difference scheme. V. A second-order sequel to godunov's method, J. Comput. Phys. 32 (1979) 101–136.
[15] P. Colella, P. R. Woodward, The piecewise parabolic method (PPM) for gas-dynamical simulations, J. Comput. Phys. 54 (1984) 174–201.
[16] E. F. Toro, Riemann Solvers and Numerical Methods for Fluid Dynamics: A Practical Introduction, Springer, Berlin, 2009.
[17] R. Courant, E. Isaacson, M. Rees, On the solution of nonlinear hyperbolic differential equations by finite differences, Comm. Pure Appl. Math. 5 (1952) 243–255.
[18] A. Harten, High resolution schemes for hyperbolic conservation laws, J. Comput. Phys. 49 (1983) 357–393.
[19] A. Harten, B. Engquist, S. Osher, S. R. Chakravarthy, Uniformly high order accurate essentially nonoscillatory schemes, III, J. Comput. Phys. 71 (1987) 231–303.
[20] X. D. Liu, S. Osher, T. Chan, Weighted essentially non-oscillatory schemes, J. Comput. Phys. 115 (1994) 200–212.
[21] A. Jameson, W. Schmidt, E. L. I. Turkel, Numerical solution of the Euler equations by finite volume methods using Runge-Kutta time stepping schemes, AIAA Paper 81-1259.
[22] E. Tadmor, Convergence of spectral methods for nonlinear conservation laws, SIAM J. Numer. Anal. 26 (1989) 30–44.
[23] A. W. Cook, W. H. Cabot, A high-wavenumber viscosity for high-resolution numerical methods, J. Comput. Phys. 195 (2004) 594–601.
[24] A. W. Cook, W. H. Cabot, Hyperviscosity for shock-turbulence interactions, J. Comput. Phys. 203 (2005) 379–385.
[25] A. Harten, The artificial compression method for computation of shocks and contact discontinuities. III. Self-adjusting hybrid schemes, Math. Comput. 32 (1978) 363–389.
[26] H. C. Yee, N. D. Sandham, M. J. Djomehri, Low-dissipative high-order shock-capturing methods using characteristic-based filters, J. Comput. Phys. 150 (1999) 199–238.
[27] E. Garnier, P. Sagaut, M. Deville, A class of explicit ENO filters with application to unsteady flows, J. Comput. Phys. 170 (2001) 184–204.
[28] H. C. Yee, B. Sjögreen, Development of low dissipative high order filter schemes for multiscale Navier-Stokes/MHD systems, J. Comput. Phys. 225 (2007) 910–934.
[29] S. Lee, S. K. Lele, P. Moin, Interaction of isotropic turbulence with shock waves: effect of shock strength, J. Fluid Mech. 340 (1997) 225–247.
[30] N. A. Adams, K. Shariff, A high-resolution hybrid compact-ENO scheme for shock-turbulence interaction problems, J. Comput. Phys. 127 (1996) 27–51.
[31] S. Pirozzoli, Conservative hybrid compact-WENO schemes for shock-turbulence interaction, J. Comput. Phys. 178 (2002) 81–117.
[32] Y. X. Ren, M. E. Liu, H. X. Zhang, A characteristic-wise hybrid compact-WENO scheme for solving hyperbolic conservation laws, J. Comput. Phys. 192 (2003) 365–386.
[33] J. Wang, L. P. Wang, Z. Xiao, Y. Shi, S. Chen, A hybrid numerical simulation of isotropic compressible turbulence, J. Comput. Phys. 229 (2010) 5257–5279.
[34] S. Pirozzoli, Numerical methods for high-speed flows, Annu. Rev. Fluid Mech. 43 (2011) 163–194.
[35] Q. Zhou, Z. H. Yao, F. He, M. Y. Shen, A new family of high-order compact upwind difference schemes with good spectral resolution, J. Comput. Phys. 227 (2007) 1306–1339.
[36] D. J. Hill, D. I. Pullin, Hybrid tuned center-difference-WENO method for large eddy simulations in the presence of strong shocks, J. Comput. Phys. 194 (2004) 435–450.
[37] D. Kim, J. H. Kwon, A high-order accurate hybrid scheme using a central flux scheme and a

WENO scheme for compressible flowfield analysis, J. Comput. Phys. 210 (2005) 554–583.
[38] J. Larsson, S. K. Lele, P. Moin, Effect of numerical dissipation on the predicted spectra for compressible turbulence, Annual Research Briefs (2007) 47–57.
[39] R. Samtaney, D. I. Pullin, B. Kosović, Direct numerical simulation of decaying compressible turbulence and shocklet statistics, Phys. Fluids 13 (2001) 1415–1430.
[40] J. C. Wang, Y. P. Shi, L. P. Wang, Z. L. Xiao, X. T. He, S. Y. Chen, Effect of shocklets on the velocity gradients in highly compressible isotropic turbulence, Phys. Fluids 23.
[41] J. C. Wang, Y. P. Shi, L. P. Wang, Z. L. Xiao, X. T. He, S. Y. Chen, Effect of compressibility on the small-scale structures in isotropic turbulence, J. Fluid Mech. 713 (2012) 588–631.
[42] J. C. Wang, Y. P. Shi, L. P. Wang, Z. L. Xiao, X. T. He, S. Y. Chen, Scaling and statistics in three-dimensional compressible turbulence, Phys. Rev. Lett. 108 (2012) 214505.
[43] Y. T. Yang, J. C. Wang, Y. P. Shi, Z. L. Xiao, X. T. He, S. Y. Chen, Interactions between inertial particles and shocklets in compressible turbulent flow, Phys. Fluids 26 (2014) 091702.
[44] S. Y. Chen, Z. H. Xia, J. C. Wang, Y. T. Yang, Recent progress in compressible turbulence, Acta Mech. Sin. 31 (2015) 275–291.
[45] P. Sagaut, C. Cambon, Homogeneous Turbulence Dynamics, Cambridge University Press, Cambridge, 2008.
[46] S. Lee, S. K. Lele, P. Moin, Eddy shocklets in decaying compressible turbulence, Phys. Fluids A 3 (4) (1991) 657–664.
[47] C. Federrath, On the universality of supersonic turbulence, Monthly Notices of the Royal Astronomical Society 436 (2013) 1245–1257.
[48] S. Jagannathan, D. A. Donzis, Reynolds and Mach number scaling in solenoidally-forced compressible turbulence using high-resolution direct numerical-simulations, J. Fluid Mech. 789 (2016) 669–707.
[49] S. Pirozzoli, F. Grasso, Direct numerical simulations of isotropic compressible turbulence: Influence of compressibility on dynamics and structures, Phys. Fluids 16 (2004) 4386–4407.
[50] K. Lee, S. S. Girimaji, J. Kerimo, Effect of compressibility on turbulent velocity gradients and small-scale structure, J. Turbul. 10 (2009) 1–18.
[51] Z. H. Xia, Y. P. Shi, Q. Q. Zhang, S. Y. Chen, Modulation to compressible homogenous turbulence by heavy point particles. I. Effect of particles' density, Phys. Fluids 28 (2016) 016103.
[52] D. M. Sutherland, The viscosity of gases and molecular force, Philos. Mag. 5 (1893) 507–531.
[53] A. N. Kolmogorov, The local structure of turbulence in incompressible viscous fluid for very large Reynolds number, Dokl. Akad. Nauk SSSR 30 (1941) 301–305.
[54] D. S. Balsara, C. W. Shu, Monotonicity preserving weighted essentially non-oscillatory schemes with increasingly high order of accuracy, J. Comput. Phys. 160 (2000) 405–452.
[55] S. K. Lele, Compact finite-difference schemes with spectral-like resolution, J. Comput. Phys. 103 (1992) 16–42.
[56] S. Y. Chen, G. D. Doolen, R. H. Kraichnan, Z. S. She, On statistical correlations between velocity increments and locally averaged dissipation in homogeneous turbulence, Phys. Fluids 5 (1993) 458.
[57] C. W. Shu, S. Osher, Efficient implementation of essentially non-oscillatory shock-capturing schemes, J. Comput. Phys. 77 (1988) 439–471.
[58] P. D. Lax, Weak solutions of nonlinear hyperbolic equations and their numerical computation, Comm. Pure Appl. Math. 7 (1954) 159–193.
[59] A. Harten, S. Osher, B. Engquist, S. R. Chakravarthy, Some results on uniformly high-order accurate essentially nonoscillatory schemes, Appl. Numer. Math. 2 (1986) 347–377.
[60] L. Fu, X. Y. Hu, N. A. Adams, A family of high-order targeted ENO schemes for

compressible-fluid simulations, J. Comput. Phys. 305 (2016) 333–359.
[61] D. S. Balsara, S. Garain, C. W. Shu, An efficient class of WENO schemes with adaptive order, J. Comput. Phys. 326 (2016) 780–804.
[62] V. A. Titarev, E. F. Toro, Finite-volume WENO schemes for three-dimensional conservation laws, J. Comput. Phys. 201 (2004) 238–260.
[63] G. A. Gerolymos, D. Snchal, I. Vallet, Very-high-order WENO schemes, J. Comput. Phys. 228 (2009) 8481–8524.
[64] X. X. Zhang, C. W. Shu, Positivity-preserving high order finite difference WENO schemes for compressible Euler equations, J. Comput. Phys. 231 (2012) 2245–2258.
[65] X. Y. Hu, N. A. Adams, C. W. Shu, Positivity-preserving method for high-order conservative schemes solving compressible Euler equations, J. Comput. Phys. 242 (2013) 169–180.
[66] C. W. Shu, High order WENO and DG methods for time-dependent convection-dominated pdes: A brief survey of several recent developments, J. Comput. Phys. 316 (2016) 598–613.
[67] Y. T. Yang, J. C. Wang, Y. P. Shi, Z. L. Xiao, X. T. He, S. Y. Chen, Acceleration of passive tracers in compressible turbulent flow, Phys. Rev. Lett. 110 (6) (2013) 064503.
[68] J. C. Wang, Y. P. Shi, L. P. Wang, Z. L. Xiao, X. T. He, S. Y. Chen, Scaling and statistics in three-dimensional compressible turbulence, Phys. Rev. Lett. 108 (2012) 214505.
[69] N. A. Phillips, An example of non-linear computational instability. In: B. Bolin (ed.) The Atmosphere and the Sea in Motion, pp. 501–504. Oxford Univ. Press, Oxford, 1959.
[70] P. L. Roe, Approximate Riemann solvers, parameter vectors, and difference schemes, J. Comput. Phys. 43 (1981) 357–372.